Supporting information

Control over Near-Ballistic Electron Transport through Formation of Parallel Pathways in a Single-Molecule Wire

Albert C. Aragonès,[†,‡] Nadim Darwish,[#] Simone Ciampi,[#] Li Jiang,[⊥] Raphael Roesch,[¶] Eliseo Ruiz,[*,‡,§] Christian A. Nijhuis,[*,⊥,‖] and Ismael Díez-Pérez[*,†]

[†] Department of Chemistry, Faculty of Natural & Mathematical Sciences, King's College London, Britannia House, 7 Trinity Street, London SE1 1DB, United Kingdom

[‡] Institut de Química Teòrica i Computacional (IQTC), Universitat de Barcelona, Diagonal 645, 08028 Barcelona, Spain

[§] Departament de Química Inorgànica i Orgànica, Universitat de Barcelona, Diagonal 645, 08028 Barcelona, Spain

[#] School of Molecular and Life Sciences, Curtin University, Bentley WA 6102, Australia

[⊥] Department of Chemistry, National University of Singapore, 3 Science Drive 3, Singapore 117543

[‖] Centre for Advanced 2D Materials, National University of Singapore, 6 Science Drive 2, Singapore 117546

[¶] Center for Biosensors and Bioelectronics, Biodesign Institute, Arizona State University, Tempe, Arizona 85287, United States.

Table of Contents

1. Synthetic details……..…S3

2. Technical details of the single-molecule transport measurements……..…S8

3. Additional single-molecule conductance data.

- **3.1. Ferrocene dissolved in mesitylene**……..S9
- **3.2. Ferrocene dissolved in toluene**……..S10
- **3.3. Linear histogram of the BFc junction**.....S12
- **3.4. 1-D Histograms without data selection and rejected data**.S12

4. 2D conductance and plateau length histograms…..……..S13

5. Temperature-dependent single-molecule measurements……..S15

6. Computational methods and additional calculations……..S17

- **6.1. Transmission calculations**……..S18
- **6.2. Full MO diagrams for BFc, TFc and BFc-butadiyne**……..S20

7. Sample preparation……S22

8. References……..S22

1. Synthetic details

Materials and methods for *1,4-Diferrocenyl-1,3-butadiyne* (BFc-butadiyne).

All chemicals, unless noted otherwise, were of analytical grade and used as received. Solvents for chemical reactions and chromatographic purification procedures were redistilled prior to use. Merck 60 Å silica gel (220−400 mesh particle size) was used for column chromatography. Unless otherwise specified NMR spectra were recorded on a Bruker Avance 400 spectrometer in deuteriochloroform (CDCl3 from Aldrich, passed through basic aluminum oxide) using the residual solvent signal as internal reference. Gas chromatography-mass spectrometry (GC-MS) analyses were performed by means of an *Agilent* Technologies 7890A GC system equipped with a HP-5 capillary column (5% phenyl methyl siloxan, 30 m × 250 □m × 0.25 □m) and interfaced with an Agilent 5975N MSD scheme operating in electron impact (EI) mode. The flow rate of the helium carrier gas was 14 mL/min and a temperature program from 80 °C to 280 °C at a ramping rate of 15 °C/min was used. The column was held at the initial temperature for 5 min and the final temperature was then held for an additional 20 min. When noted, the total ion current chromatograms of the GC/MS **station** were used to monitor extent of conversions and to assay the purity of synthesized compounds and commercial precursors (*Note*: the ion current is a function of the compound characteristics and it is not a true quantification). High-resolution mass spectral data (HRMS) were obtained using a Waters Xevo QTof MS via ESI experiments and infusing the sample at 8 □L/min.

1,4-Diferrocenyl-1,3-butadiyne (BFc-butadiyne). Triethylamine (300 □l, 2.2 mmol) was added at

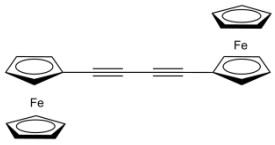

room temperature in small portions over 5 min to a stirred suspension of ethynylferrocene (200 mg, 0.95 mmol) and copper(II) chloride dehydrate (5 mg, 0.03 mmol) in toluene (ca. 25 mL). The suspension was stirred at 100 °C in air for 24 h. The solution was filtered and the filtrate dried in vacuo. The crude material was purified by silica gel column chromatography (ethyl acetate/hexane, 1/1, v/v) to give the pure title compound as a red solid (150 mg, 38%). 1H NMR (400 MHz, CDCl3): □ 4.51 p.p.m. (bs, 4 H), 4.27 (bs, 14 H); 13C NMR (100 MHz, CDCl3): □ 79.1, 72.1, 70.9, 70.2, 69.2, 63.7; MS (EI, 70 eV), m/z (rel intensity): 418 (100) [M]+, 416 (14), 239 (16), 209 (10), 121 (12); HRMS (m/z): $[M+H]^+$ calcd for $C_{24}H_{19}Fe_2$, 419.0186; found 419.0182.

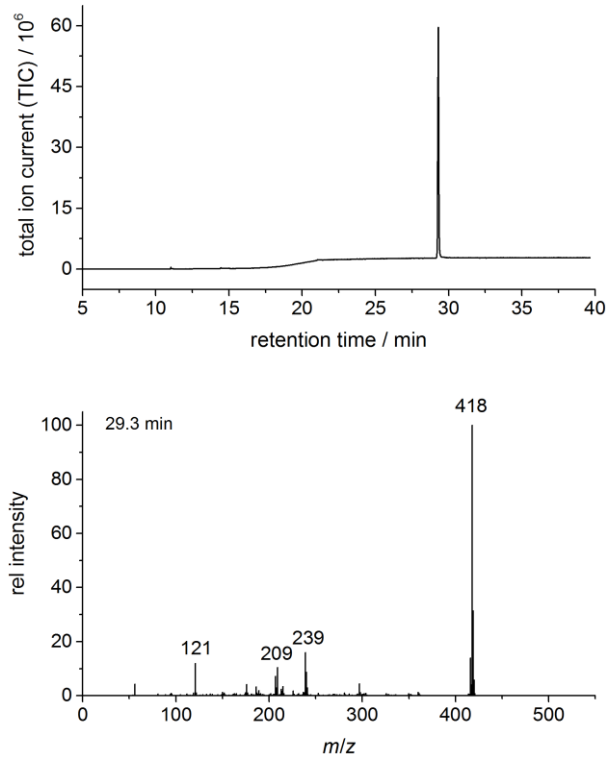

Fig. S1.1 *Plot of the total GC-MS ion current chromatogram and normalized mass profile at the specified elution time for* ***BFc-butadiyne****.*

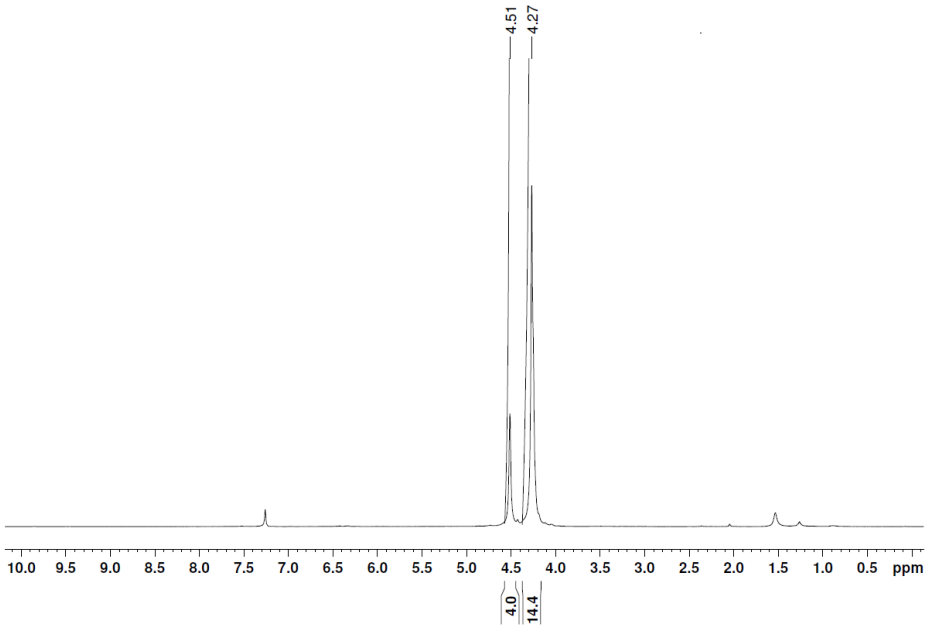

Fig. S1.2 *^{1}H NMR spectrum (400 MHz, $CDCl_3$) of BFc-butadiyne.*

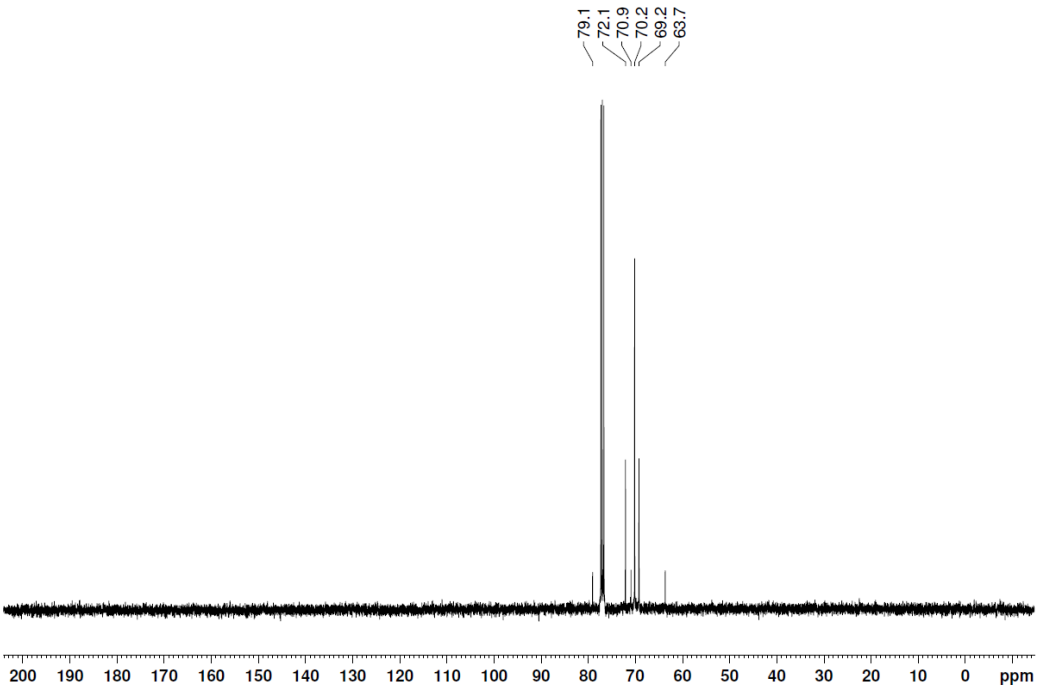

Fig. S1.3 *^{13}C NMR spectrum (1 00 MHz, $CDCl_3$) of BFc-butadiyne.*

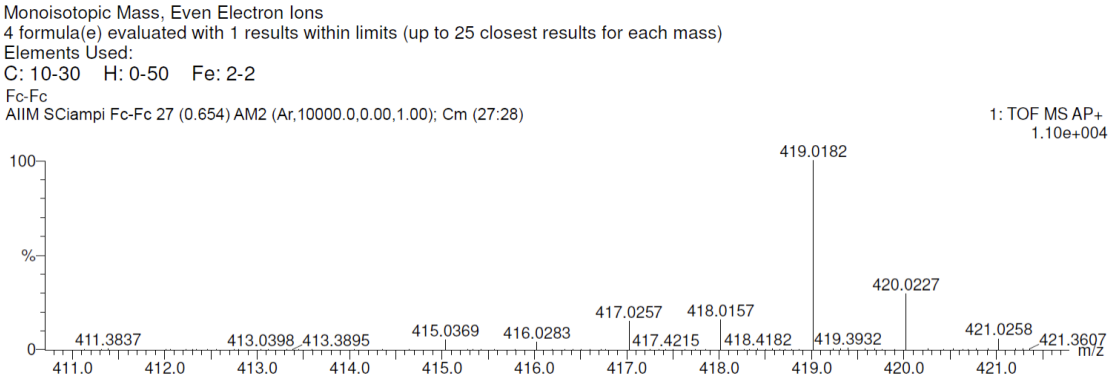

Minimum:				-1.5			
Maximum:		5.0	200.0	120.0			
Mass	Calc. Mass	mDa	PPM	DBE	i-FIT	i-FIT (Norm)	Formula
419.0182	419.0186	-0.4	-1.0	15.5	168.9	0.0	C24 H19 Fe2

Fig. S1.4 *HRMS of BFc-butadiyne.*

Materials and methods for BFc and TFc.

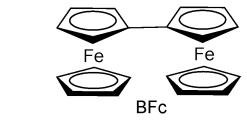

BFc

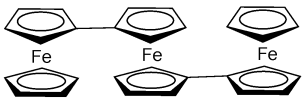

TFc

We used the Ullmann reaction reported in the literature[1] to synthesize BFc and TFc in one pot by reacting iodoferrocene 1.00 g (3.2 mmol), 1,1'-diiodoferrocene 1.41g (3.2 mmol) along with activated copper powder 10.00 g (161 mol) in a 50 mL round bottom flaks. The reaction mixture was deoxygenated using 3 freeze-pump-thaw cycles. Then the melted mixture was stirred at 140 °C for 20 hours. After re-cooling to room temperature, the brown solid mixture was washed by toluene until the toluene was the colorless. The organic phase was concentrated by using rotary evaporation to obtain crude orange product. The crude product was purified by column chromatography (hexane/toluene=4/1) to provide 0.45 g BFc (the second band) in 38% yield as a yellow solid and 0.13 g TFc (the third band) in 13% yield as a yellow solid (the first band was ferrocene). BFc: ^{1}H NMR (300 MHz, CDCl3): δ 4.36 (t, 4 H, J=1.8 Hz), 4.17 (t, 4H, J=1.8 Hz), 4.00 (s, 10 H); ^{13}C NMR (75 MHz, CDCl3): δ 84.2, 69.2, 67.6, 66.3; ESI-MS (m/z): 370.3 [M]+. TFc: ^{1}H NMR (300 MHz, CDCl3): δ 4.17 (t, 4 H), 4.06 (t, 4 H), 4.04 (br, 4 H), 3.97 (br, 4 H), 3.87 (s, 10 H); ^{13}C NMR (75 MHz, CDCl3): δ 68.1, 67.9, 66.6, 66.4, 65.2; ESI-MS (m/z): 554.1 [M]+

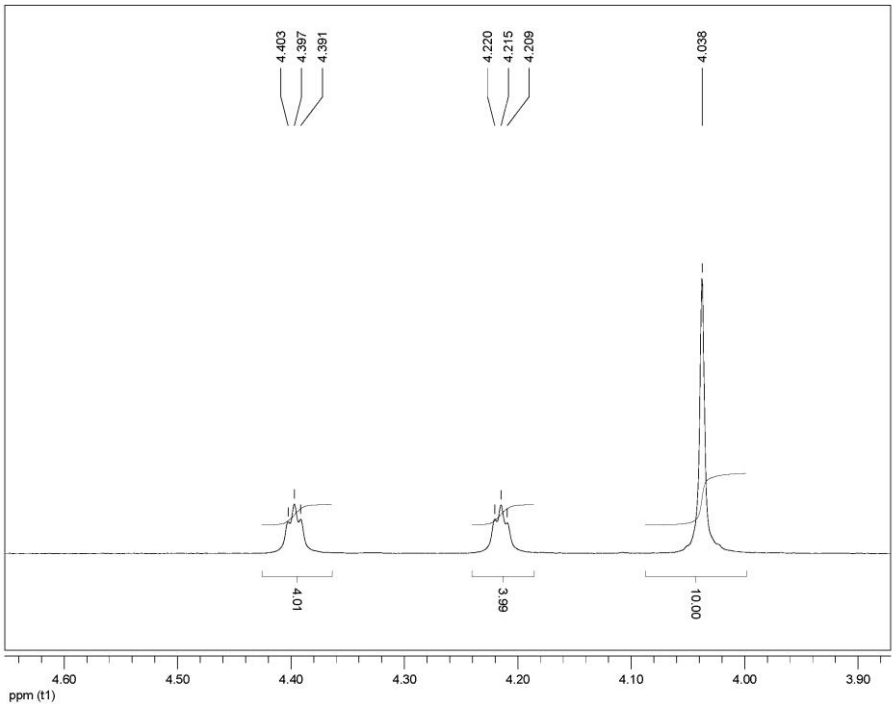

Fig. S1.5 *^{1}H NMR spectrum (400 MHz, $CDCl_3$) of* ***BFc****.*

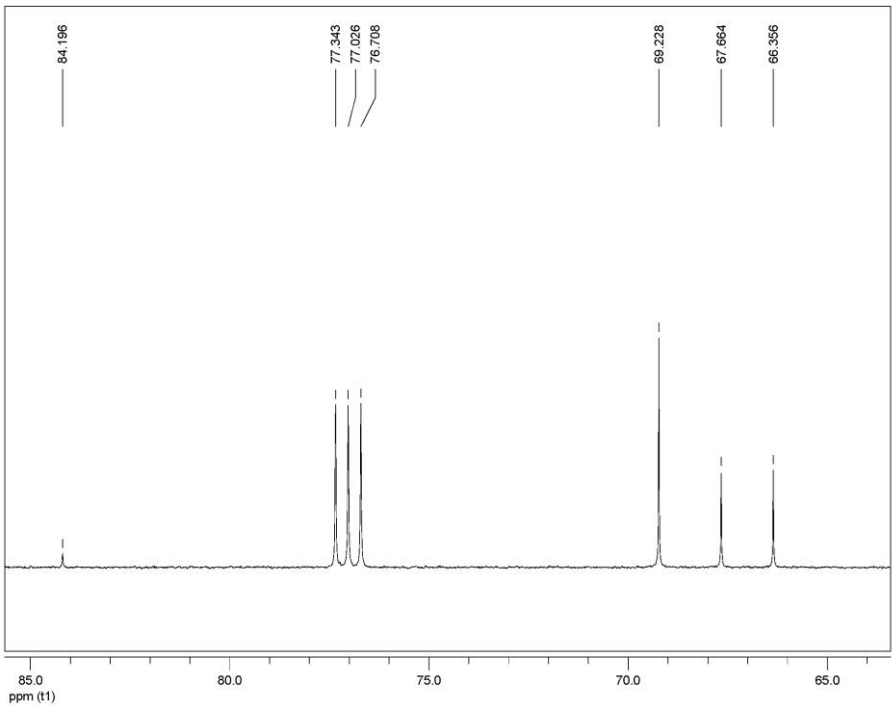

Fig. S1.6 *^{1}C NMR spectrum (100 MHz, $CDCl_3$) of* ***BFc****.*

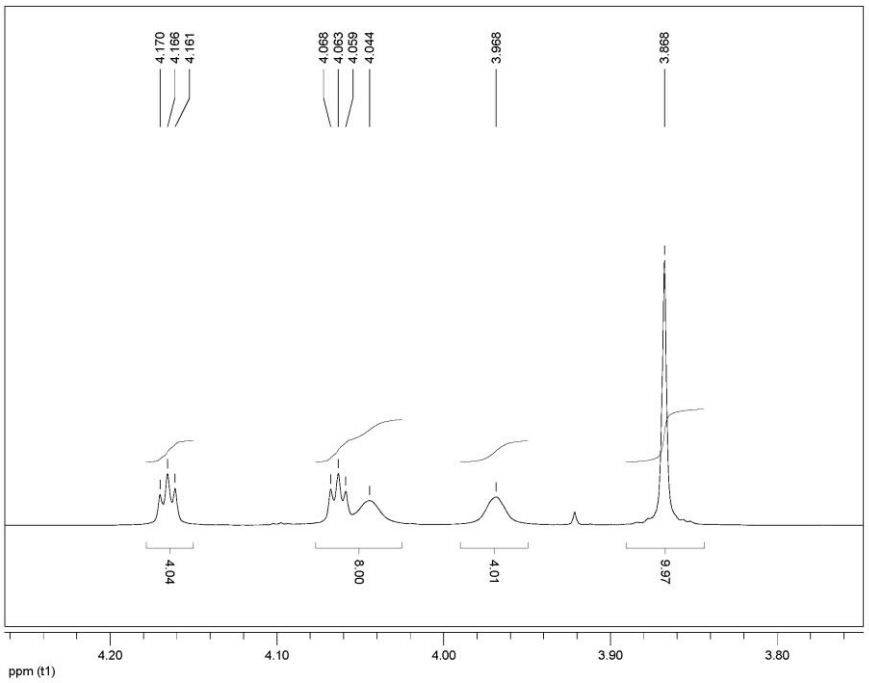

Fig. S1.7 *^{1}H NMR spectrum (400 MHz, $CDCl_3$) of* ***TFc****.*

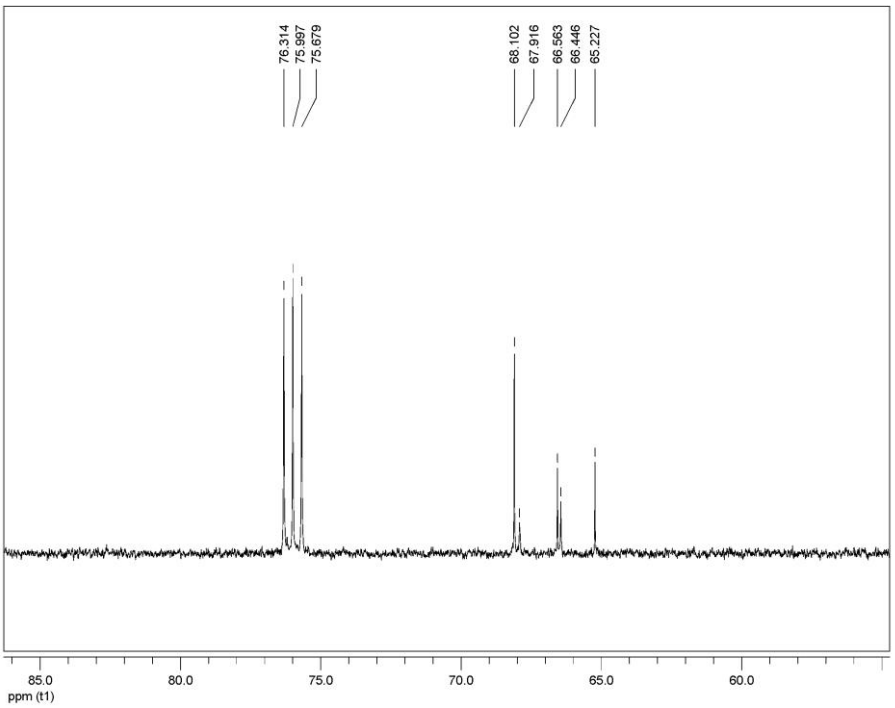

Fig. S1.8 *^{1}C NMR spectrum (100 MHz, $CDCl_3$) of* ***TFc****.*

2. Technical details of the single-molecule transport measurements

Details about the STM-break junction technique have been published elsewhere[2]. All the conductance measurements were carried out with a mechanically and electronically isolated PicoSPM I microscope head controlled by a Picoscan-2500 electronics (all from Agilent) and using a homemade PTFE STM cell. Data captures were acquired using a NI-DAQmx/BNC-2110 National Instruments (LabVIEW data acquisition System) and analyzed with LabVIEW code. The procedure of a typical break-junction experiment is based on bringing the STM tip to tunneling distance over a flat clean Au (111) surface area as a first step. The STM feedback is then turned off and the tip is driven into and out of contact with the substrate at a speed of 1-2V/s. This 2-points feedback loop is used to capture thousands of current decays (4000-5000). Single molecule conductance (G) was determined using the expression $G=I_{step}/V_{BIAS}$, where I is the current and V is the voltage difference between the two junction electrodes. The current decays are accumulated to semi-logarithmic conductance histograms. The observed plateaus in the individual current decays result in the observed peaks in the conductance histograms and provide an averaged value of the single-molecule conductance. Transient curves that are either noisy or that showed smooth exponential decay because of the absence of molecular bridge formation were rejected when building the histograms using an automatic selection procedure driven by a code written in LabVIEW. The histograms were compiled by applying the same automated selection criteria to each set of the recorded decay curves. The selection procedure allows current traces showing counts exceeding a defined threshold to be added to the conductance histogram. The percentage decay curves that showed clear molecular steps were typically 15–20% and were all selected to build the histograms.[3–5] This selection process made peaks in the 1D conductance histograms more prominent (or regions with a higher number of

counts in the 2D maps) above the tunneling background and also allowed a quantitative measure of the yield of molecular junction formation in all of the conductance traces.

All 2D logarithmic maps were performed by a code written in LabVIEW. The counting maps are built from the captured current decays, accumulating the collected counts in the selected conductance sections of the whole measured conductance range[6]. The same selection criteria used to build the analogous 1D histograms were employed.

We built the cross-correlation conductance map of Fig. 3a following similar procedures used in references [67,68] in the manuscript. They were built using an automatic algorithm, which segments the captured conductance range in different regions under study (Y-axis bins). In such delimited region, the algorithm analyses the captures inside the specific bin only and, as a consequence, only the counts of the current decays containing plateaus inside the region are accumulated and plotted in the X-axis. The key point of the method is that when a plateau is detected and the complete current trace contains more plateaus in conductance ranges different to the studied one, they are accumulated and showed in the 2D map, thus highlighting the interdependence between the occurrences of the different plateaus.

3. Additional single-molecule conductance data

We work with highly diluted solutions of the target molecules to avoid compact layer formation, dimerization or other aggregation phenomena. This procedure was followed to avoid interference with the single-molecule measurement.[7–10]

With the aim to avoid conductance features due the interaction of the electrodes with the working medium, different solvents were tested. The single-molecule measurements were measured in different solvents (see subsections below). The conductance values of the different Fc-oligomers do not show significant dependence on the used solvents most likely due to weak interactions with the medium.[11]

3.1. Ferrocene dissolved in mesitylene

Some solvent molecules like mesitylene can show single-molecule features at 0.1 G_o (inset Fig. S3.1.1)[12], close to the values of our measured Fc-oligomers. These features are significantly reduced with the presence of molecules of higher affinity to the Au electrodes such as Fc (Fig. S3.1.1). However, to avoid any interferences with the conductance features coming from the solvent, we decided to explore other solvents in this occasion (see next section).

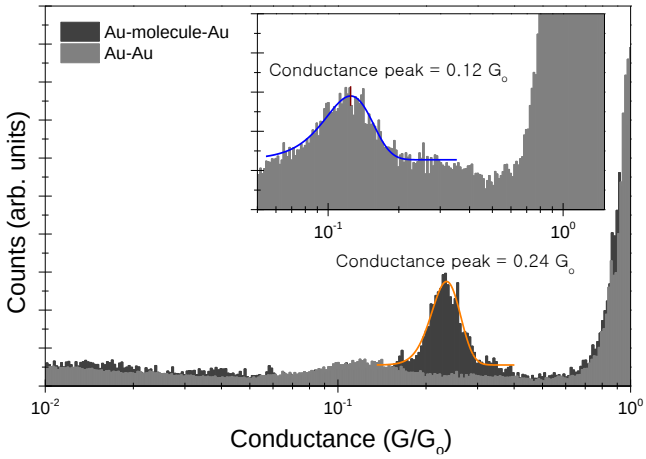

Fig.S3.1.1 *Semi-log conductance histograms for Fc in mesitylene (dark grey) and in the absence of Fc (light grey). Inset zoom shows a detail of the conductance peak for the latter. The conductance values are extracted from Gaussian fits of the peaks. The applied bias was set to 8 mV.*

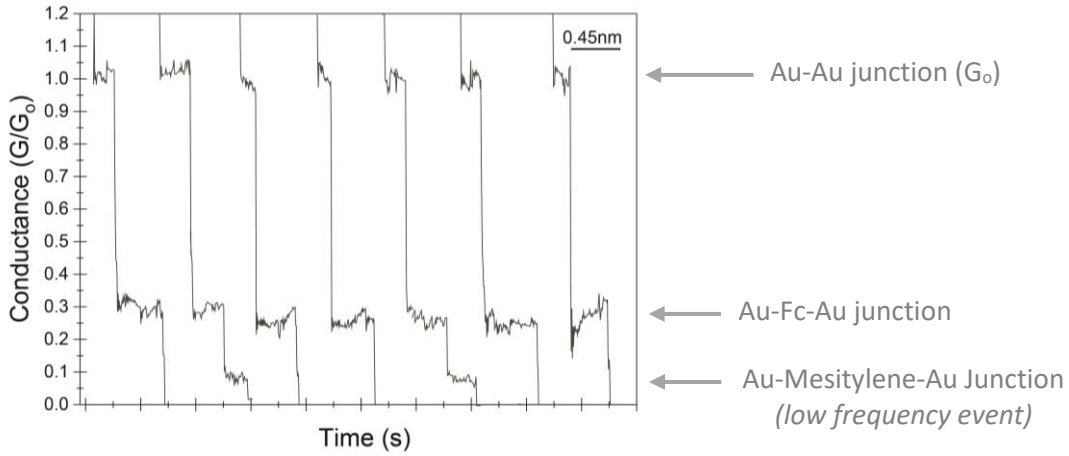

Fig.S3.1.2 *Representative individual current traces displaying plateau features for the Fc in mesitylene used to build the histograms of Fig.S3.1.1 (dark grey). The applied bias was set to 8 mV.*

3.2. Ferrocene dissolved in toluene

Despite toluene does not show any single-molecule conductance feature within the employed current range (Figs. S3.2.1 and 3.2.2),[12] it was not used as the working medium due to its higher vapor pressure as opposed to mesitylene and 1,2,4-trichlorobenzene solvents. Same conductance values were obtained as compared to mesitylene.

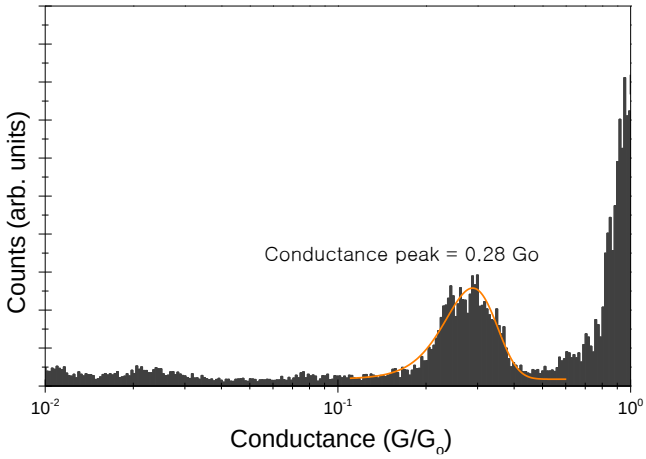

Fig.S3.2.1 *Semi-log conductance histogram for Fc in toluene. The conductance value is extracted from Gaussian fits of the peaks. The applied bias was set to 8 mV.*

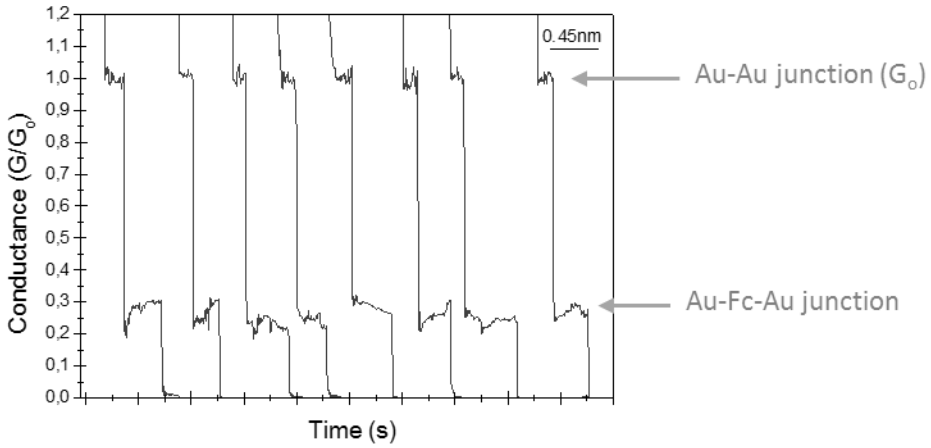

Fig.S3.2.2 *Representative individual current traces displaying plateau features for Fc in toluene used to build the histograms of Fig.S3.2.1. The applied bias was set to 8 mV. Note that no low G features coming from the solvent (see Fig. S3.1.2) are not observed in this solvent.*

3.3. Linear histogram of the BFc junction

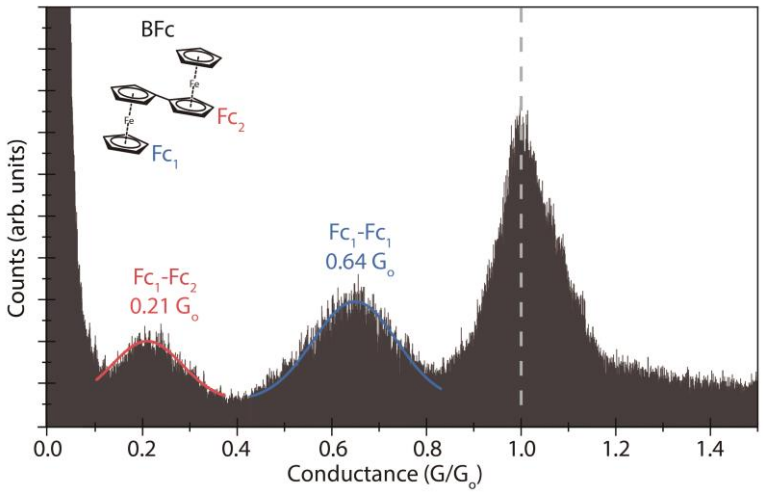

Fig.S3.3.1 *1D conductance histogram for the BFc junction represented in linear scale including the $1G_0$ feature. The applied bias was set to 8 mV.*

3.4. 1-D Histograms without data selection and rejected data

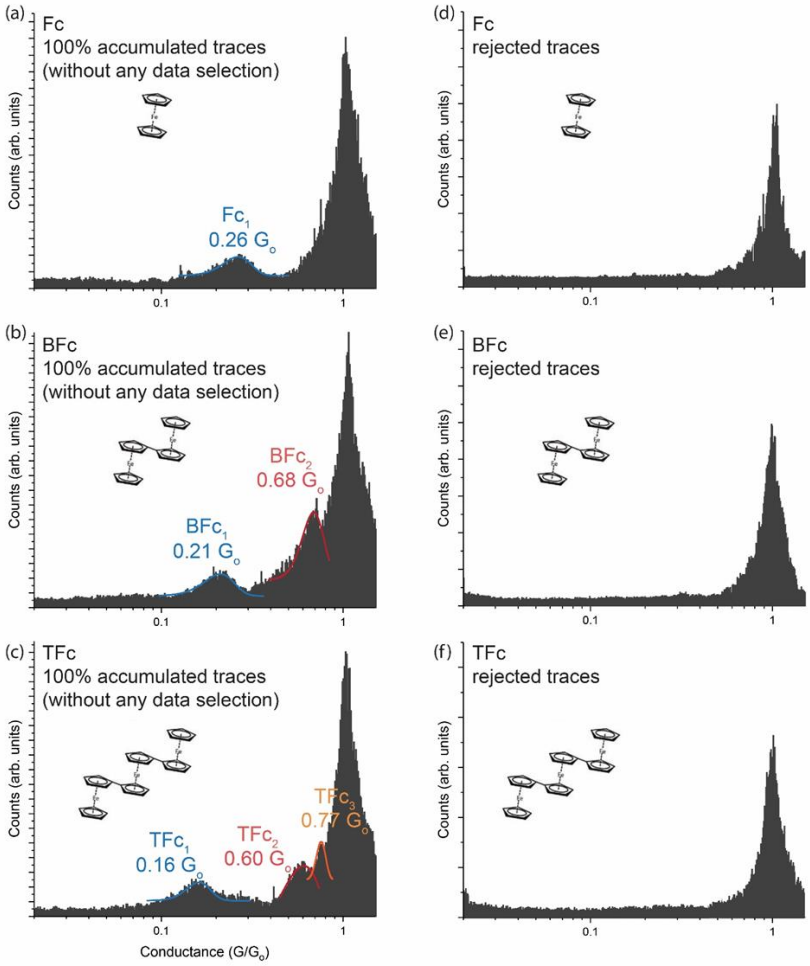

Fig.S3.4.1 *1D conductance histogram (a-c) without any data selection for Fc, BFc and TFc. 1 D conductance histograms accumulating the rejected curves from the histograms of Fig. 2 of the manuscript.*

4. 2D conductance and plateau length histograms

2D maps were built by accumulating all individual pulling traces without any data selection (Fig. S4.1). The extracted average step length for all plateaus (see step length histograms in Fig. S4.2) results in a constant value that slightly oscillates between 0.25 and 0.3 nm without any clear trend versus the molecular length (see the clearest comparison between BFc and BFc-butadiyne, Fig. S4.2b-e). Moreover, this value cannot be directly related to any relevant structural length from the DFT-relaxed structure (see Fig. S4.3). Such results support the presented picture of sequentially Fc disconnections where the vertical displacement of the STM tip to break each single Fc bridge (plateaus in the individual traces) is related to the Fc-Au interaction force rather than to any relevant molecular distance.

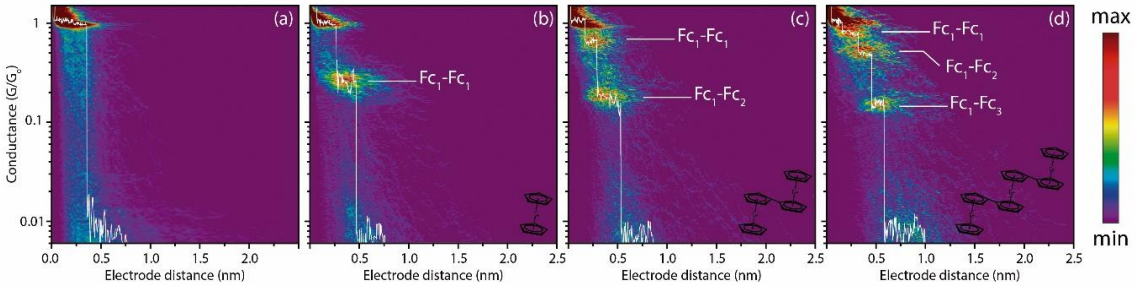

Fig.S4.1 *2D maps built from few thousands of individual current captures without any data selection for the BFc molecule. The white trace is a representative individual capture. The applied bias was set to 10 mV.*

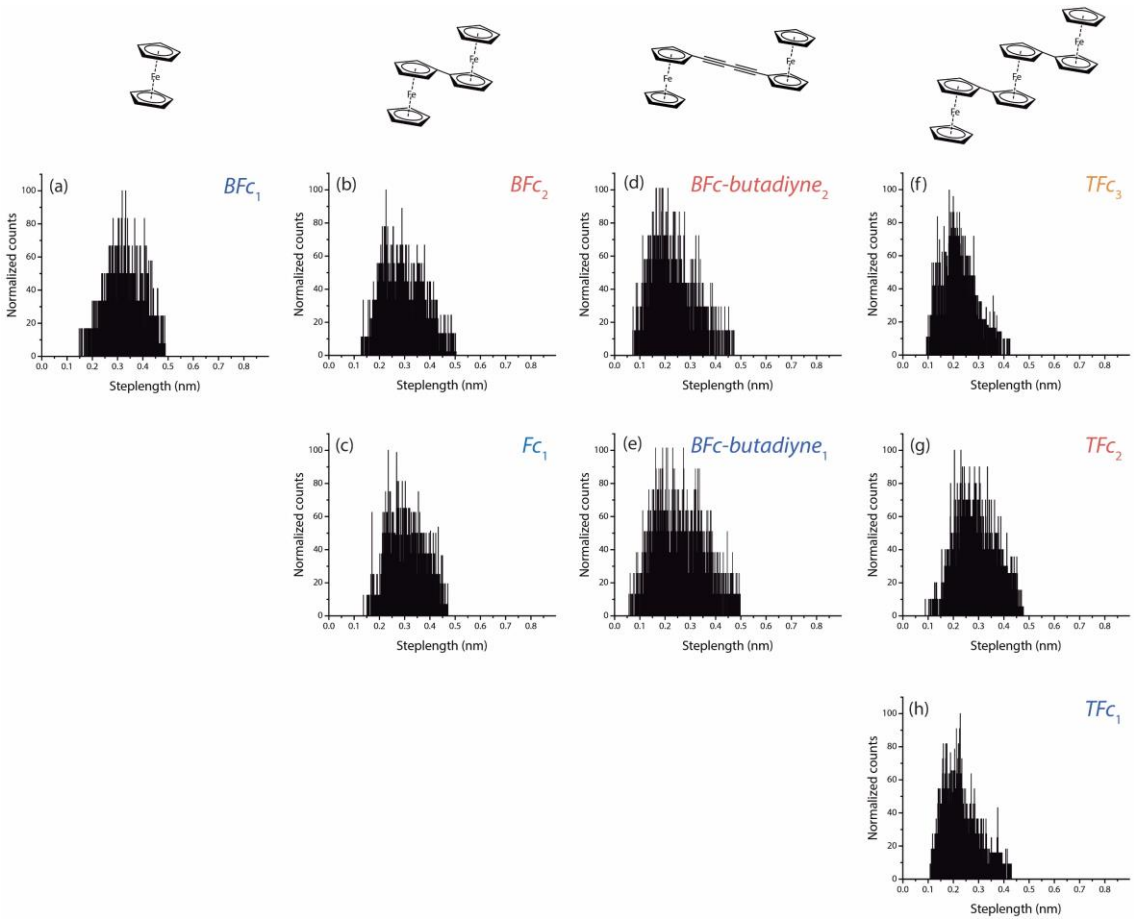

Fig.S4.2 *Plateau length histograms for all the observed conductance features in the single-molecule junctions built with Fc (a), BFc (b-c), BFc-butadiyne (d-e) and TFc (f-h).*

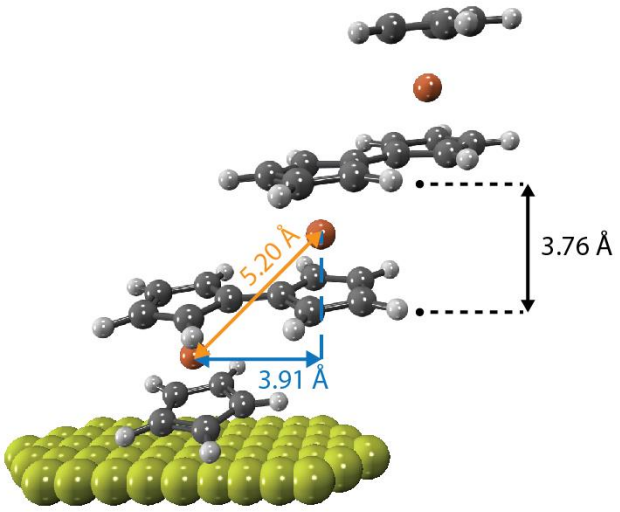

Fig.S4.3 *DFT-relaxed structure of the TFc compound together with the important distances.*

5. Temperature-dependent single-molecule measurements

Figure S5.1 to S5.4 shows representative histograms at different working temperatures for Fc, BFc, TFc and BFc-butadiyne wires respectively in 1,2,4-trichlorobenzene. Figure S5.5 shows the plot of G mean versus temperature for the BFc-butadiyne molecule.

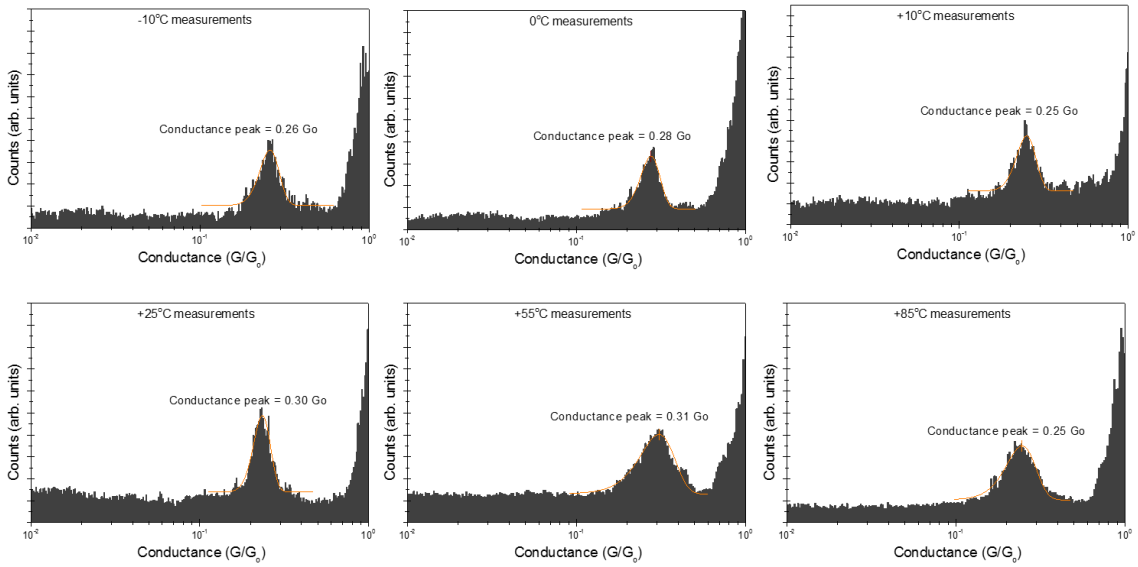

Fig.S5.1 *Semi-log conductance histograms for the Fc molecule in 1,2,4-trichlorobenzene at different temperatures (labeled in the figure). The conductance values are extracted from Gaussian fits of the peaks. The applied bias was set to 10 mV.*

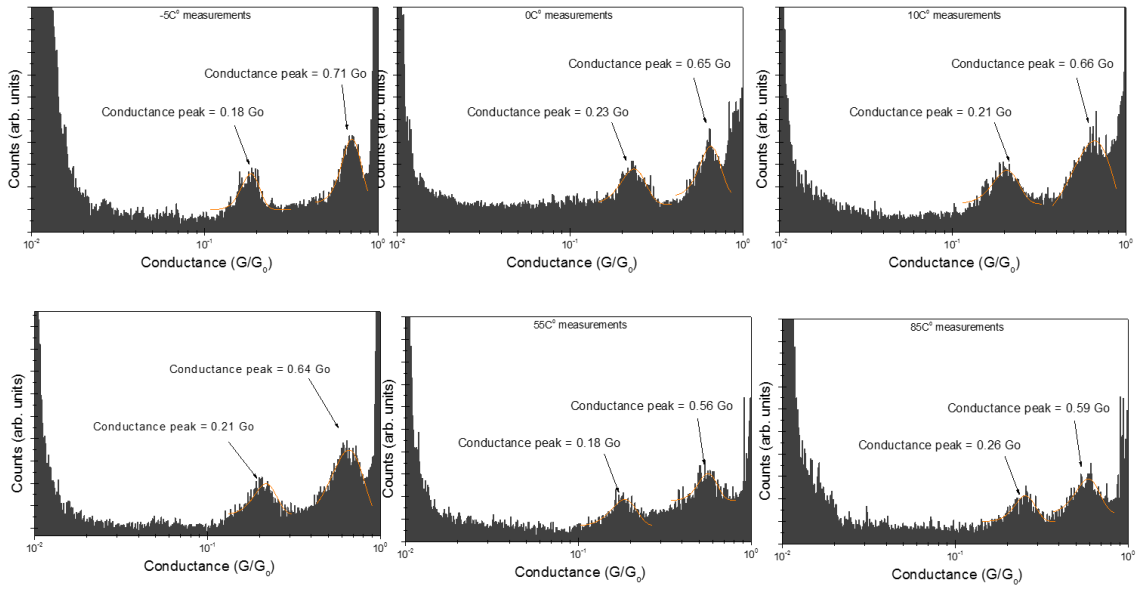

Fig.S5.2 *Semi-log conductance histograms for the BFc molecule in 1,2,4-trichlorobenzene at different temperatures (labeled in the figure). The conductance values are extracted from Gaussian fits of the peaks. The applied bias was set to 10 mV. The tail appearing at low conductance corresponds to the background current of the used current amplifier.*

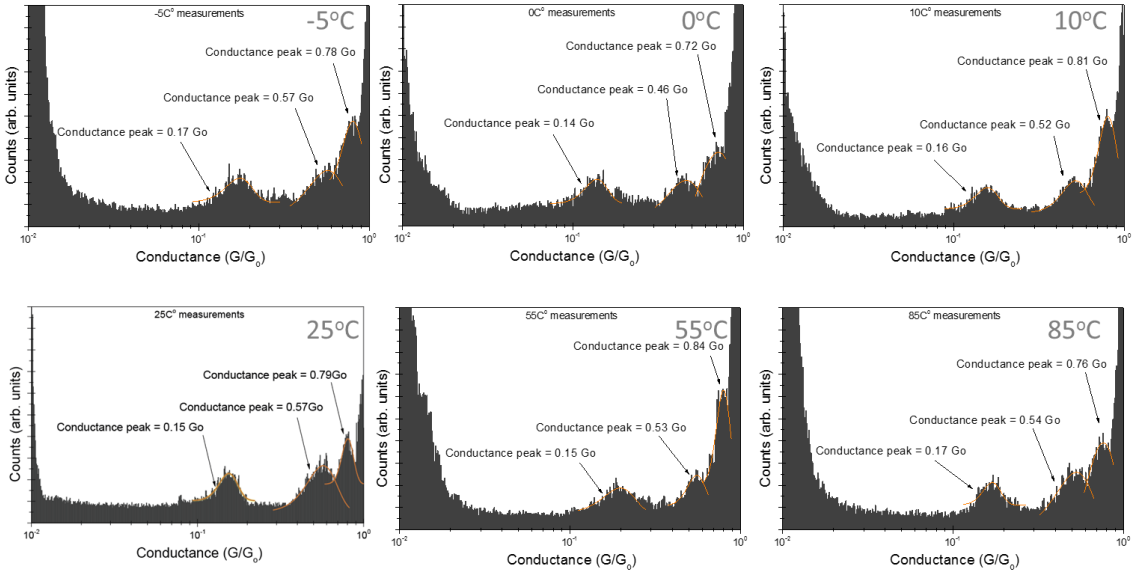

Fig.S5.3 *Semi-log conductance histograms for the TFc molecule in 1,2,4 trichlorobenzene at different temperatures (labeled in the figure). The conductance values are extracted from Gaussian fits of the peaks. The applied bias was set to 10 mV. The tail appearing at low conductance corresponds to the background current of the used current amplifier.*

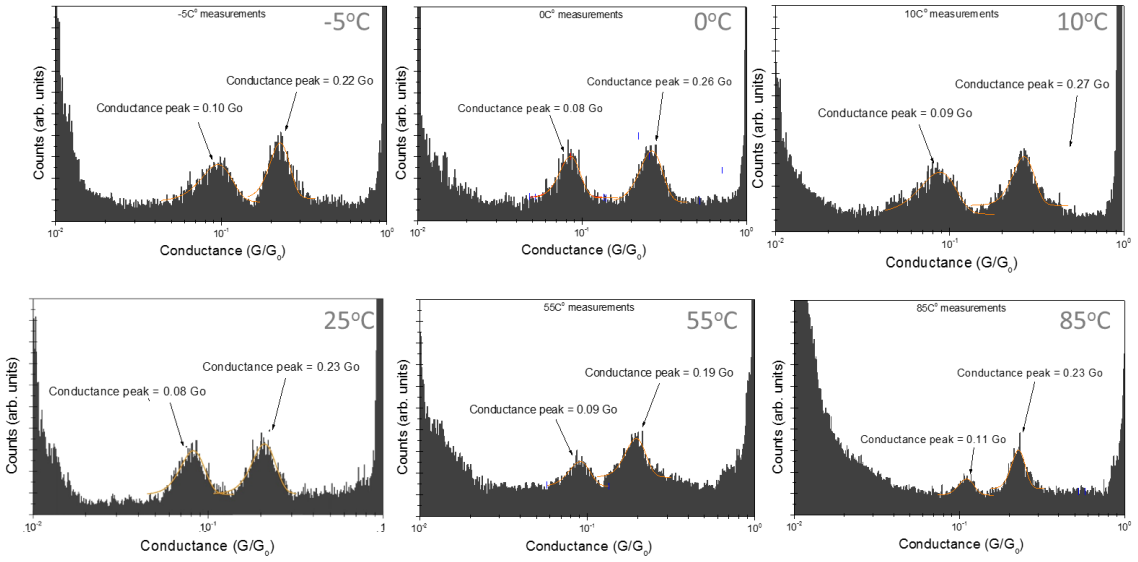

Fig.S5.4 *Semi-log conductance histograms for the BFc-butadiyne molecule in 1,2,4 trichlorobenzene at different temperatures (labeled in the figure). The conductance values are extracted from Gaussian fits of the peaks. The applied bias was set to 10 mV. The tail appearing at low conductance corresponds to the background current of the used current amplifier.*

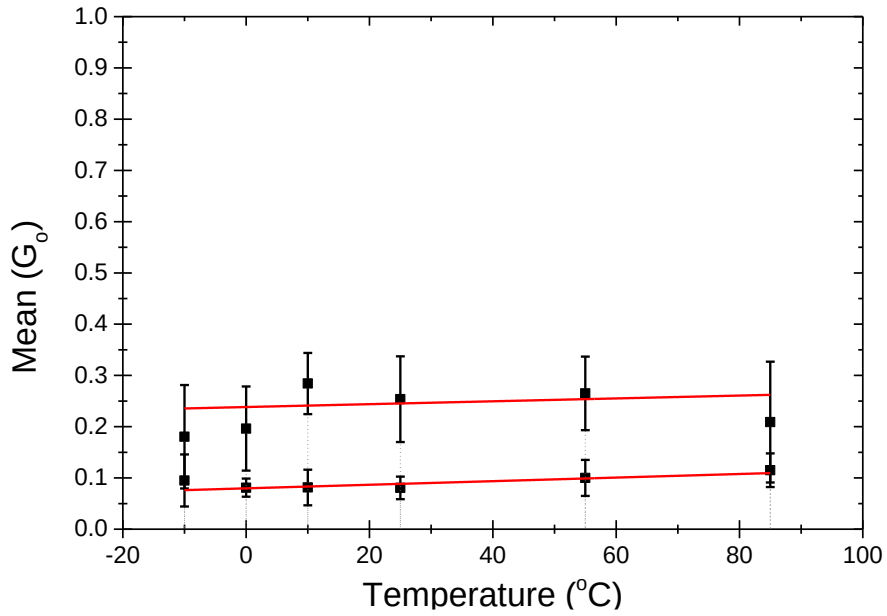

Fig.S5.5 *Plot of BFc-butadiyne G versus the working temperature. Error bars represent the standard deviation of all the acquired data sets extracted from the FWHM of the histogram peaks.*

6. Computational Methods and additional calculations

Orbitals visualization. The geometry optimizations and calculated frontier orbitals were performed using Density Functional theory (DFT) at the B3LYP/TZV level.[13–15] All the orbital computational calculations and representations were performed using the software package *Gaussian 09.*[16]

The Fc unit eclipsed conformation (D_{5h} symmetry) constitutes the equilibrium point and it has been used to perform computational calculations. The staggered (D_{5d} symmetry) represents the saddle-point to the internal rotation of the ligand rings.[17–19] The energy difference between both possible conformations is about few meV, which means the two cyclopentane rings can freely rotate at room temperature.[17,20] Frequency calculations was employed to check the energy minima of the structures. In the Fc-oligomers, BFc, Bc-butadiyne and TFc, the steric hindrance results in a more stable *trans*- conformation versus the Fc units as obtained in the geometry-optimization for all the calculated backbones.[21–23] All the structures have been represented in the trans- and Fc-eclipsed conformations.

Transmission probability. DFT-optimization of the structures were performed to determine the molecule-electrode distances with the all-electron FHI-aims computer code[24] using numerical local orbital basis set. This approach allows full-potential calculations at a low computational cost without using any approximations for the potential, such as pseudopotentials or frozen cores. The numerical "tight" basis set was employed in all calculations. The SCF parameters to reach a good convergence in the calculations were a Gaussian occupation type with a parameter of 0.01, a Pulay mixer with 10 cycles and a mixing parameter of 0.02. The dispersion terms were included in the calculations using the many-body approach[25] resulting in an optimized distance around 3.0 Å between the Cp ring and the Au(111) surface. Taking into account such optimized

DFT+dispersion distances extracted with the fhi-aims code, the STM tip was simulated by considering a molecule/electrode distance around of 2.5 Å (see Fig. S6.1 right). Transport calculations were carried out with model structures including small gold tips or flat electrodes using the ATK code (ATK computer code version 2016.3, QuantumWise A/S: 2015). An array of small gold tips composed by 10 gold atoms each (6-3-1 atoms per layer in the tip) is placed in "contact" with the molecule (see Fig. 7). Transport calculations[26] were performed using the PBE functional[27] with pseudopotentials and double zeta basis set was employed for Fe, C and H atoms while a single-zeta basis set was used for Au atoms. The scattering region is a double 4x8 2d superlattice of three layers oriented in the Au(111) face. A very large grid of k-points (35x35) must be employed to calculate the transmission spectra and the conductance values. The use of a smaller set of k-points leads to an unrealistic large contribution to the transmission close to the Fermi level, especially in the cases with flat electrodes.

6.1. Transmission calculations

We have studied if the shape of the electrodes plays a significant role in the transport calculations. In the case of the TFc, we have analysed the effect of the tip shape with two different junction models (see Fig. S6.1): the first one is an array of pyramidal tips contacting each Fc unit. Such structure might originate because of the Au interacting with the cyclopentadienyl (Cp) ring in combination with mechanical pulling (see also Fig. 7). The second one is the TFc molecule sandwiched between two perfectly flat electrodes in its most stable configuration (lying flat) as supported by fhi-aims calculations. DFT geometry optimizations indicates that the molecule-electrode interaction has the general tendency to maximize the contact area between both electrodes, and that the Au-molecule interaction is mainly through the C-H groups in the flat electrodes model, whereas in the tips array electrodes the Au-molecule contact goes essentially via the π system of the Cp ligands. The calculated conductance values at the experimental bias voltage (0.05V) are an order of magnitude lower than those obtained in the "multiple-tips" scenario: 0.02, 0.04 and 0.06 for Fc, BFc and TFc, respectively (Fig. S6.2a-c). The results also show an additive effect that does not follow the saturation behaviour observed in the experimental conductance trend, which is otherwise captured in the "multiple-tips" model. In part, such saturating trend displayed in the "multiple-tips" scenario can be explained by the slight mismatch between the Fc position in the molecule and the Au lattice, resulting in non-equivalent contacts for the three electrode-Fc adducts.

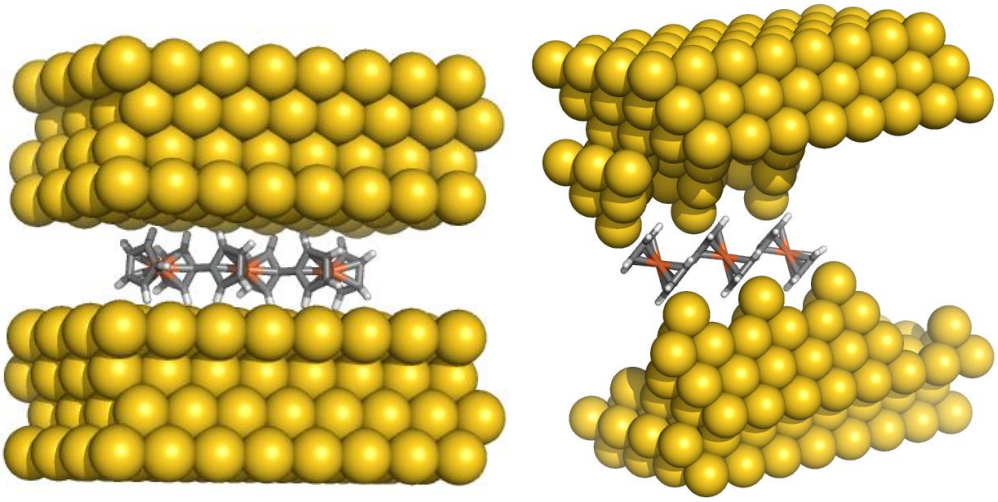

Fig.S6.1 *Two calculated junction structures for the transmission function of TFc: flat electrodes (left panel) and tips array (right panel).*

Representative transmission curves of two proposed scenrios are shown in Fig. S6.2. The more irregular structure of the electrode-molecule contacts in the "multiple-tips" model produces an artefactual peak around -0.3 eV (Fig. S6.2d-f). The analysis of the transmission eigenfunctions of such peak (not shown) indicated a main contribution of gold with a weak contribution of the occupied frontier levels of the TFc (similar results are found for BFc and Fc, see Fig. S6.2c-d). The sharp features below the Fermi level are ascribed to the transmission through the molecular moiety, which present high contributions from the metal d_{xy} and d_{x2-y2} orbitals as expected due to the electronic structure of these molecules.

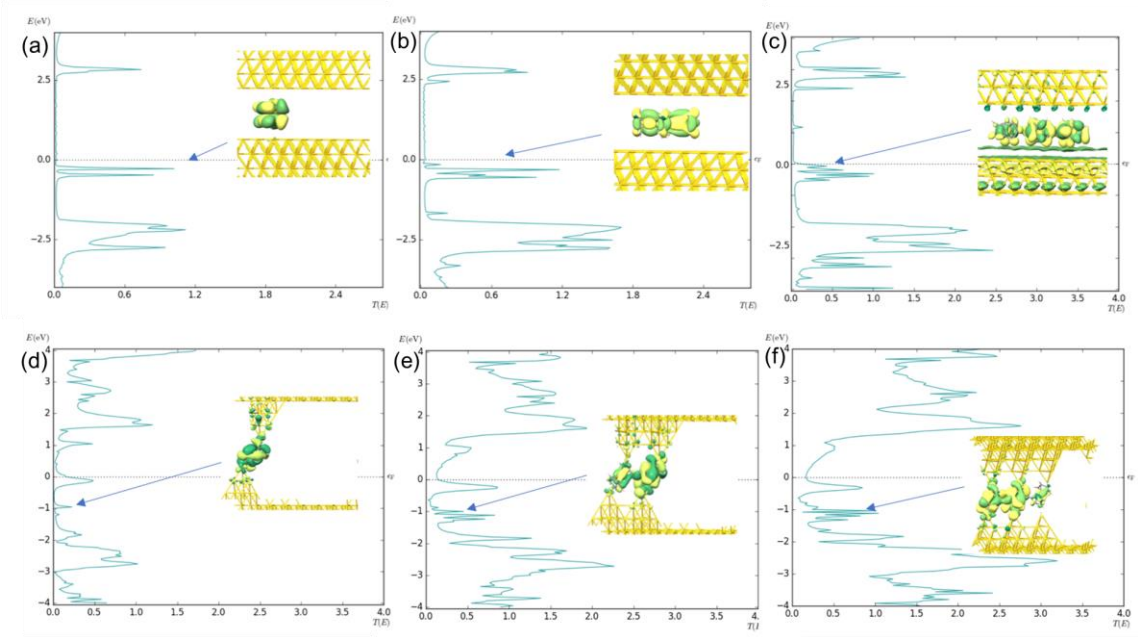

Fig.S6.2 *Transmission probability function of the Fc, BFc and TFc systems showing the effect of using different junction configurations: (a-c) flat electrodes and (b) multiple-tips electrodes. All transmission eigenfunctions correspond to the closest molecular contribution to the Fermi level. The transmission eigenstates are obtained by diagonalizing the transmission matrix and the corresponding eigenvalues indicate the importance of each eigenstate in the transport. As it is a complex wavefunction, the color*

map indicating the phase of the function is represented from 0 to 2π by dark green to yellow. The value employed for the isosurface is 0.3.

6.2. Full MO diagrams for BFc, TFc and BFc-butadiyne

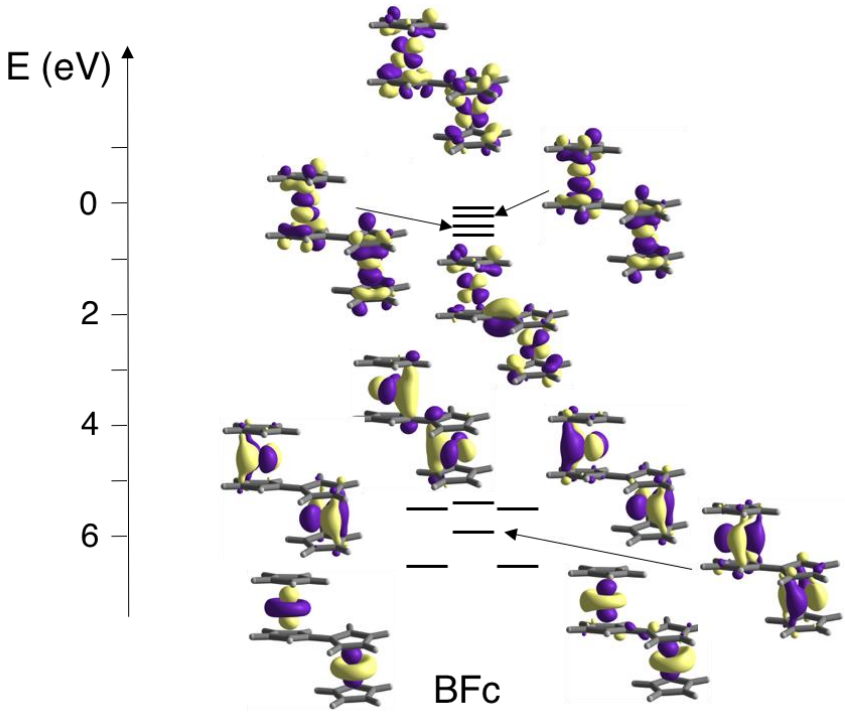

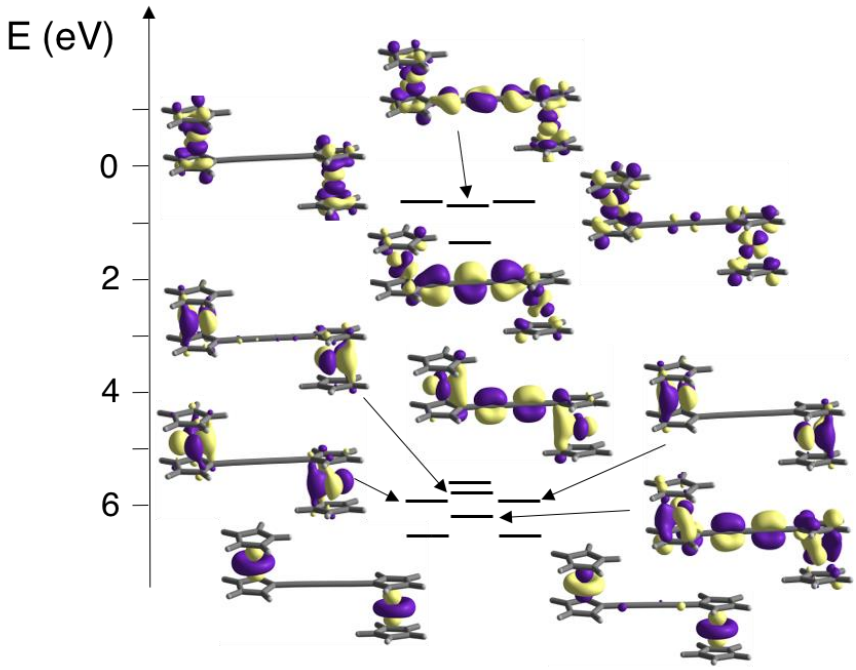

BFc-butadiyne

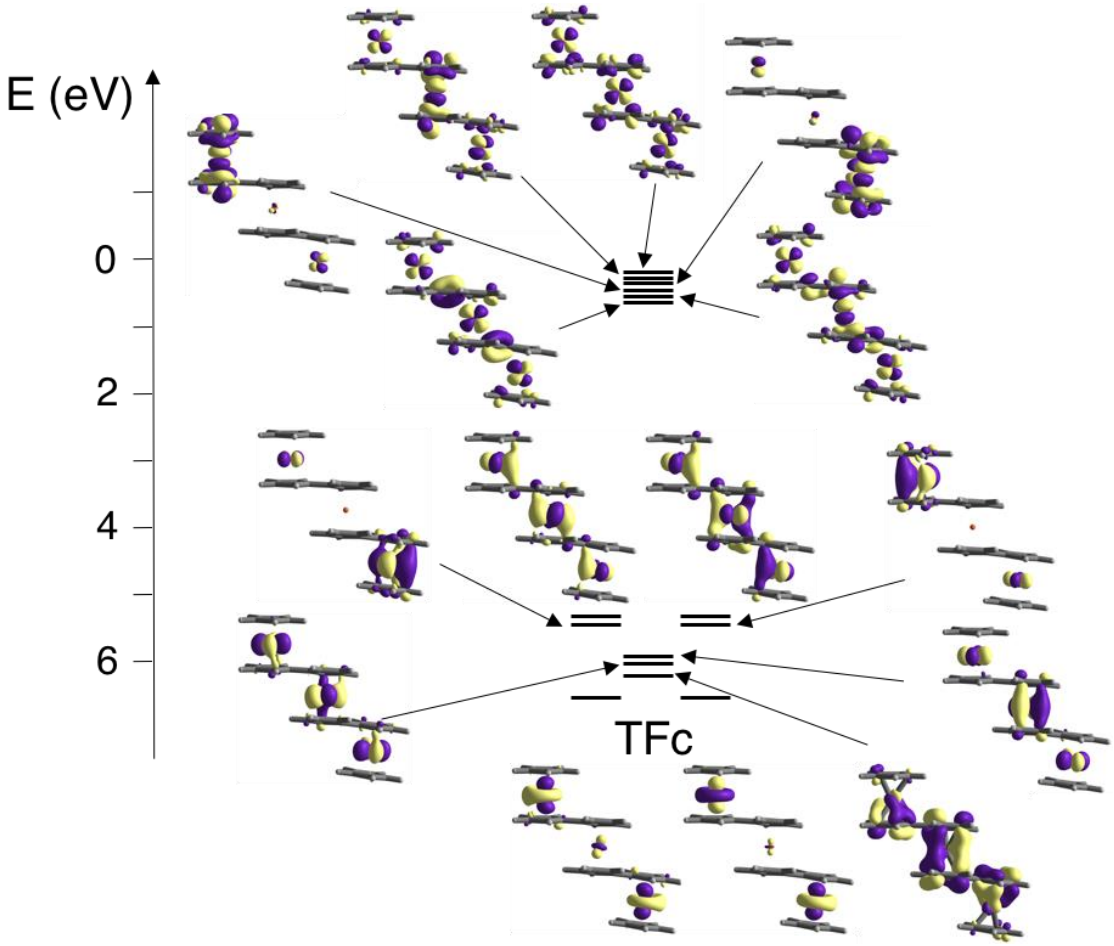

7. Sample preparation

An Au (111) monocrystalline substrate (10 mm x 1 mm) of 99.9999% purity and orientation accuracy < 0.1 degrees was purchased from MaTeck (Germany). The Au (111) monocrystalline substrate was electropolished to eliminate possible residual contaminants and then was annealed with a H_2 flame. The Au (111) substrate was then introduced in the STM PTFE cell, which then was filled with an 80 μL of pure 1,2,4-trichlorobenzene (Sigma-Aldrich), where STM junction control experiments were firstly run. 3 drops of a μM 1,2,4-trichlorbenzene solution of the ferrocene compounds were then added to STM cell before starting the break junction experiments. All glassware and PTFE STM cells were cleaned with piranha solution (3:1 H_2SO_4/H_2O_2 by volume) before usage, followed by rinsing with 18 MΩ cm^{-1} Milli-Q water (Millipore).

8. References

1 P. V. Roling and M. D. Rausch, *J. Org. Chem.*, 1972, **37**, 729–732.

2 B. Xu and N. J. Tao, *Science*, 2003, **301**, 1221–3.

3 Li, J. Hihath, F. Chen, T. Masuda, L. Zang and Tao, *J. Am. Chem. Soc.*, 2007, **129**, 11535–11542.

4 T. Hines, I. Díez-Pérez, H. Nakamura, T. Shimazaki, Y. Asai and N. Tao, *J. Am. Chem. Soc.*, 2013, **135**, 3319–22.

5 A. C. A. C. Aragonès, D. Aravena, J. I. J. I. Cerdá, Z. Acís-Castillo, H. Li, J. A. J. A. Real, F. Sanz, J. Hihath, E. Ruiz and I. Díez-Pérez, *Nano Lett.*, 2016, **16**, 218–226.

6 Z. Balogh, P. Makk and A. Halbritter, *Beilstein J. Nanotechnol.*, 2015, **6**, 1369–76.

7 D. Welipitiya, P. A. Dowben, J. Zhang, W. W. Pai and J. F. Wendelken, *Surf. Sci.*, 1996, **367**, 20–32.

8 R. F. Dou, D. Y. Zhong, W. C. Wang, K. Wedeking, G. Erker, L. Chi and H. Fuchs, *J. Phys. Chem. C*, 2007, **111**, 12139–12144.

9 C. M. Woodbridge, D. L. Pugmire, R. C. Johnson, N. M. Boag and M. A. Langell, *J. Phys. Chem. B*, 2000, **104**, 3085–3093.

10 D. Y. Zhong, H. Peng, J. Franke, T. Blömker, G. Erker, L. F. Chi and H. Fuchs, *Nano Lett.*, 2009, **9**, 132–6.

11 E. Leary, H. Höbenreich, S. J. Higgins, H. van Zalinge, W. Haiss, R. J. Nichols, C. M. Finch, I. Grace, C. J. Lambert, R. McGrath and J. Smerdon, *Phys. Rev. Lett.*, 2009, **102**, 86801.

12 S. Afsari, Z. Li and E. Borguet, *Angew. Chemie Int. Ed.*, 2014, **53**, 9771–9774.

13 W. Koch and M. C. Holthausen, *A Chemist's Guide to Density Functional Theory*, Wiley-VCH Verlag GmbH, Weinheim, FRG, 2001, vol. 3.

14 A. Savin, *Recent Developments and Applications of Modern Density Functional Theory*, 1996, vol. 4.

15 R. Ditchfield, *J. Chem. Phys.*, 1971, **54**, 724.

16 M. J. Frisch, G. W. Trucks, H. B. Schlegel, G. E. Scuseria, M. A. Robb, J. R. Cheeseman, G. Scalmani, V. Barone, B. Mennucci, G. A. Petersson, H. Nakatsuji, M. Caricato, X. Li, H. P. Hratchian, A. F. Izmaylov, J. Bloino, G. Zheng, J. L. Sonnenberg, M. Hada, M. Ehara, K. Toyota, R. Fukuda, J. Hasegawa, M. Ishida, T. Nakajima, Y. Honda, O. Kitao, H. Nakai, T. Vreven, J. A. Montgomery Jr., J. E. Peralta, F. Ogliaro, M. Bearpark, J. J. Heyd, E. Brothers, K. N. Kudin, V. N. Staroverov, R. Kobayashi, J. Normand, K. Raghavachari, A. Rendell, J. C. Burant, S. S. Iyengar, J. Tomasi, M. Cossi, N. Rega, J. M. Millam, M. Klene, J. E. Knox, J. B. Cross, V. Bakken, C. Adamo, J. Jaramillo, R. Gomperts, R. E. Stratmann, O. Yazyev, A. J. Austin, R. Cammi, C. Pomelli, J. W. Ochterski, R. L. Martin, K. Morokuma, V. G. Zakrzewski, G. A. Voth, P. Salvador, J. J. Dannenberg, S. Dapprich, A. D. Daniels, Ö. Farkas, J. B. Foresman, J. V Ortiz, J. Cioslowski and D. J. Fox, *Gaussian Inc Wallingford CT*, 2009, 34, Wallingford CT.

17 S. Coriani, A. Haaland, T. Helgaker and P. Jørgensen, *ChemPhysChem*, 2006, **7**, 245–249.

18 C. Morari, I. Rungger, A. R. Rocha, S. Sanvito, S. Melinte and G.-M. Rignanese, *ACS Nano*, 2009, **3**, 4137–4143.

19 M. Ormaza, P. Abufager, N. Bachellier, R. Robles, M. Verot, T. Le Bahers, M.-L. Bocquet, N. Lorente and L. Limot, *J. Phys. Chem. Lett.*, 2015, **6**, 395–400.

20 A. Haaland, J. E. Nilsson, T. Olson and T. Norin, *Acta Chem. Scand.*, 1968, **22**, 2653–2670.

21 R. C. Quardokus, N. A. Wasio, R. P. Forrest, C. S. Lent, S. A. Corcelli, J. A. Christie, K. W. Henderson and S. A. Kandel, *Phys. Chem. Chem. Phys.*, 2013, **15**, 6973–81.

22 M. Kotora, D. Nečas and P. Štěpnička, *Collect. Czechoslov. Chem. Commun.*, 2003, **68**, 1897–1903.

23 K.-F. Braun, V. Iancu, N. Pertaya, K.-H. Rieder and S.-W. Hla, *Phys. Rev. Lett.*, 2006, **96**, 246102.

24 V. Blum, R. Gehrke, F. Hanke, P. Havu, V. Havu, X. Ren, K. Reuter and M. Scheffler, *Comput. Phys. Commun.*, 2009, **180**, 2175–2196.

25 A. Tkatchenko, R. A. DiStasio, R. Car and M. Scheffler, *Phys. Rev. Lett.*, 2012, **108**, 236402.

26 M. Brandbyge, J.-L. Mozos, P. Ordejón, J. Taylor and K. Stokbro, *Phys. Rev. B*, 2002, **65**, 165401.

27 J. P. Perdew, K. Burke and M. Ernzerhof, *Phys. Rev. Lett.*, 1996, **77**, 3865–3868.

28 B. Bröker, R.-P. Blum, J. Frisch, A. Vollmer, O. T. Hofmann, R. Rieger, K. Müllen, J. P. Rabe, E. Zojer and N. Koch, *Appl. Phys. Lett.*, 2008, **93**, 243303.

29 T. Yelin, R. Korytár, N. Sukenik, R. Vardimon, B. Kumar, C. Nuckolls, F. Evers and O. Tal, *Nat. Mater.*, 2016, **15**, 444–449.